THE JOURNAL OF COMPARATIVE NEUROLOGY 413:619–633 (1999)

Dendrites of Classes of Hippocampal Neurons Differ in Structural Complexity and Branching Patterns

R.C. CANNON,[1]* H.V. WHEAL,[1] AND D.A. TURNER[2]
[1]Neuroscience Research Group, School of Biological Sciences, Southampton University, Southampton, SO16 7PX, United Kingdom
[2]Neurosurgery and Neurobiology, Duke University Medical School and Durham VAMC, Durham, North Carolina 27710

ABSTRACT

Dendrites of reconstructed hippocampal neurons were analyzed for morphometric, topologic, and fractal parameters (n = 32 quantities) to investigate neuronal groupings and growth characteristics with a common set of assumptions. The structures studied included CA1 and CA3 pyramidal cells, interneurons, and granule cells from young animals (71 cells in total). Most of the cells showed no characteristic fractal dimension; rather, the scaling relation could be well represented by a two-parameter fit, of which one parameter showed a significant difference between cell classes. Other significant quantities that differentiated cell classes were related to the complexity of the dendritic tree (number of branch points and maximal terminal branch order) and the cell's electrical properties such as the mean attenuation between the soma and terminals. Principal components analysis produced combined measures of only slightly greater discriminative power than the best individual measures, indicating that the elementary quantities capture most of the structural variation between hippocampal cell groups. Another finding was that for all cells the mean segment length increased with dendritic branch order, which is consistent with decreasing branching probability as a function of the path distance from the soma. Analysis of another set of CA1 pyramidal neurons from aged animals (n = 15; 22–24 months) showed only a few significant differences than those from young animals (n = 11; a subset of n = 71) of which the most important was a straightening of the paths between terminals and the soma. The quantities analyzed in these reconstructed hippocampal neurons may reflect both intrinsic neuronal characteristics and extrinsic influences. Hippocampal cell groupings (i.e., pyramidal cells as opposed to dentate granule cells and interneurons) were significantly differentiated by most parameters. These differences and parameter values may be critical for understanding and generating synthetic neuronal populations for modelling studies. J. Comp. Neurol. 413:619–633, 1999.

Indexing terms: morphology; three-dimensional reconstruction; fractals; morphometric analysis; hippocampus

The three-dimensional structure of neurons is of interest in understanding neuronal development and maturation, as a means of cell classification, and for understanding the complex influence of dendrites on passive and active neuronal properties (Alcantara et al., 1998; Carnevale et al., 1997; Ishizuka et al., 1995; Major et al., 1994; Mainen et al., 1996; Spruston et al., 1994; Uylings et al., 1986; Van Pelt et al., 1997). The structure of neurons is probably determined in part by inherent or genetic tendencies, such as neuronal position after migration, which is expressed early in development, and in part by later modifications resulting from a variety of environmental factors, including synaptic inputs and molecular cues such as reelin and growth factors (Alcantara et al., 1998; Nedivi et al., 1998; Zafirov et al., 1994). Whereas cell location may be determined completely by migration patterns, the resultant location of the soma and subsequent gradients of

Grant sponsor: Wellcome Trust; Grant number: NIA RO1 AG-13165; Grant sponsor: VAMC.

*Correspondence to: Robert C. Cannon, Neuroscience Research Group, School of Biological Sciences, Southampton University, Southampton SO16 7PX, UK. E-mail: rcc1@soton.ac.uk

Received 10 February 1999; Revised 22 June 1999; Accepted 21 July 1999

growth factors determine the direction and extent of dendritic projections.

The growth of dendrites has been simulated in a number of topologic (pattern of branching) and metric (length and position of branches) approaches. These approaches have the common aims of understanding and predicting some of the mechanisms and rules underlying branching patterns and of simulating neurons with realistic structure (Carriquiry et al., 1991; Ireland et al., 1985; Kliemann, 1987; Tamori, 1993; Uemura et al., 1995; Van Pelt and Verwer, 1985; Woldenberg et al., 1993). Various studies of dendrites (Li et al., 1994; Migliore et al., 1995; Pyapali and Turner, 1994, 1996; Pyapali et al., 1998b; Woldenberg et al., 1993) have also examined the variation of structure within neuronal populations under different conditions, in the hopes of determining differences that may correlate with observed single-cell and network behavior and plasticity in response to the neuronal environment. For example, dendritic plasticity after denervation or with development and senescence may indicate the neuronal response to these perturbations (Pyapali and Turner, 1994, 1996; Woldenberg et al., 1993). Realistic neuronal structures have also been used in modeling studies of single-cell behavior (Bower and Beeman, 1994; Carnevale et al., 1997; Henze et al., 1996; Migliore et al., 1995; Spruston et al., 1993; Turner, 1984a,b; Turner et al., 1991; Zador et al., 1995), and it has been shown that understanding some features of neuronal behavior demands a detailed quantitative description of a neuron's dendritic arborization. The use of such detailed information is particularly important for understanding integrative properties and electrical functioning of dendrites (Yuste and Tank, 1996).

The goal of this analysis is to quantitatively differentiate structural and functional characteristics of hippocampal neurons. Previous efforts to differentiate and contrast more than one cell type have been limited to either comparative electrotonic properties of hippocampal neurons (Carnevale et al., 1997; Turner, 1984a) or morphologic features of pyramidal cells (Ishizuka et al., 1995). However, there are many more characteristics that may be used to identify either similarities or differences between the classes of hippocampal neurons. For example, Van Pelt et al. (1997) hypothesized that the difference between more complex pyramidal neurons and less complex cells is that branching probabilities may decrease with distance from the soma more rapidly in the simpler cells than in more complex cells. Such dendrite "growing rules" may capture some characteristics of dendritic development and growth and allow simulations of dendritic development to be fairly realistic in the hope of creating accurate "synthetic" neurons.

The present analysis is based on three-dimensional reconstructions of 71 young hippocampal cells obtained from either in vivo (intact) or in vitro (slice) preparations and of 15 aged CA1 pyramidal cells, all of which are now publicly available in a worldwide web database (http://www.neuro.soton.ac.uk; Cannon et al., 1998). The neurons were all reconstructed after intracellular staining with biocytin and digitization with a Neurolucida reconstruction system (Mott et al., 1997; Pyapali and Turner, 1996; Pyapali et al., 1998a,b; Turner et al., 1995; Microbrightfield, Colchester, VT). For each of these cells, topologic, morphologic, and electrical measures have been computed. The raw data are presented, and the method of principal components analysis is used to assess which measures and combinations best correlate with known cell types. For quantities that can meaningfully be defined within a structure, such as asymmetry or branching angles, single valued measures may miss internal systematic variation. Two particular examples are considered: the branching probability and a "straightness" coefficient defined as the ratio of the physical distance of a point in the structure from the soma to its distance measured along the structure. The results support the conclusions of Van Pelt et al. (1997) that the probability of a dendrite splitting again decreases with branch order and suggest that aging may reduce the number of indirect branches in favor of those following straighter paths.

CELL STAINING AND RECONSTRUCTION METHODS

In vitro neuronal labeling

Male Fischer 344 rats, ages 22–24 months old, were killed with an overdose of halothane, as previously reported (Mott et al., 1997; Pyapali and Turner, 1996). After breathing ceased, the brain was rapidly removed and placed into cooled artificial cerebrospinal fluid [ACSF; containing (in mM) NaCl, 124; KCl, 3.25; $NaHC0_3$, 26; NaH_2PO_4, 1.25; $MgSO_4$, 2.0; $CaCl_2$, 2.4; and glucose, 10]. The hippocampi were dissected out from the whole brain and sliced in a plane transverse to the long (septotemporal) axis of the hippocampus at a thickness of 500 μm on a manual tissue chopper. Slices were maintained in ACSF in a holding chamber for approximately 2 hours and then were placed in a surface recording chamber maintained at 35°C.

All animal experiments were carried out in accordance with the NIH guidelines for the care and use of laboratory animals and were approved by the Duke University Animal Care Use Committee. All efforts were made to minimize animal suffering, to reduce the number of animals used to a minimum, and to use alternatives to in vivo techniques, including the use of in vitro slices.

Intracellular recording electrodes (1-mm thin-walled capillary glass; 90–150 MΩ) were filled with 2–4% neurobiotin (Vector Laboratories, Burlingame, CA) dissolved in 1 M potassium acetate buffer (pH 7.4). CA1 pyramidal cells and interneurons were impaled within their respective cells layer by using a hydraulic microdrive. Characteristics for a healthy impalement included a minimal resting potential of −55 mV and repetitive action potential firing in response to intracellular depolarizing pulses. The neuronal input resistance was estimated from voltage responses following the injection of hyperpolarizing current pulses 100-msec long and 0.1–0.5 nA in amplitude. After this assessment, the cells were intracellularly labeled with neurobiotin by using intracellular current stimulation (4-Hz depolarizing pulses, 150 msec in duration, 2–5 nA), with superimposed hyperpolarization (−0.2 nA) to prevent electrode blocking. Single cells near the middle of the depth of the slice were recorded to enhance the three-dimensional reconstructions (Pyapali and Turner, 1996).

In vivo neuronal labeling

Adult Sprague-Dawley rats (2–8 months old, 200–350 g, either sex) were anesthetized with urethane (1.3–1.5 g/kg, i.p.) and positioned in a stereotaxic apparatus, as previously reported (Pyapali et al., 1998a,b; Turner et al., 1995). The body temperature of the rat was kept constant by a

small-animal thermoregulation device. The scalp was removed, and a small (1.2 × 0.8 mm) bone window was drilled above the hippocampus [anteromedial edge at anteroposterior (AP) = −3.3 mm from bregma and lateral (L) = 2.2 mm] for intracellular recordings. The cisterna magna was opened, and the cerebrospinal fluid was drained to decrease pulsation of the brain. A pair of stimulating electrodes (100 μm each, with 0.5-mm tip separation) was inserted into the right fimbria-fornix [coordinates of AP = −1.3 mm, L = 1.0 mm, vertical (V) = 4.1 mm] to stimulate the commissural inputs. After the intracellular recording electrode was inserted into the brain, the bone window was covered by a mixture of paraffin and paraffin oil to prevent drying of the brain and to decrease pulsations.

Micropipettes for intracellular recordings were pulled from 2.0-mm-diameter capillary glass filled with 1 M potassium acetate in 50 mM Tris buffer (pH 7.4) also containing 3% biocytin for intracellular labeling. In vivo electrode impedances varied from 60 to 100 MΩ. Once stable intracellular recordings were obtained (Axoclamp 2B), evoked and passive physiologic properties of the cell were determined. Biocytin was then injected through a bridge circuit (Axoclamp 2B), with a 50% duty cycle of 500-msec depolarizing pulses at 0.8–2 nA for 5–60 minutes (Li et al., 1994). Postinjection survival times ranged from 2 to 18 hours.

Tissue processing of in vitro slices

Slices containing the neurobiotin-labeled cells were left in the recording chamber for 1 hour to allow active transport and diffusion of the label throughout the dendrites. The slices were then fixed overnight in 4% paraformaldehyde containing 0.1% glutaraldehyde in 0.1 M phosphate buffered saline (PBS; pH 7.4). The fixed slices were sectioned at 100 μm (nominal) on a Vibratome and collected in PBS. The 100-μm slices were found to be optimum to balance penetration of the staining reagents with a sufficiently thick section width for three-dimensional reconstructions. After three 10-minute washes in PBS and Tris buffer (TBS; pH 8.0), the sections were incubated in 1% hydrogen peroxide (H_2O_2) for 30 minutes to eliminate the endogenous peroxidase activity. After incubation, the sections were rinsed in PBS (three times, 10 minutes) and incubated overnight in avidin–biotin–horseradish peroxidase complex (ABC; Vector Laboratories) diluted in 1:200 in 1% Triton X-100 dissolved in PBS. A brown reaction product was developed after incubation of the sections in 3′-3, diaminobenzidine tetrahydrochloride (DAB; 0.03% in TBS, pH 8.0) and 0.001% H_2O_2 containing 1% nickel ammonium sulfate for intensification. The sections were air dried, dehydrated, cleared in xylene, and coverslipped (Pyapali and Turner, 1996).

Tissue processing following in vivo recordings

After 2–12-hour survival times after the intracellular labeling, the animals were given a urethane overdose and then perfused intracardially with 100 ml physiological saline followed by 400 ml of 4% paraformaldehyde, 0.1% glutaraldehyde, and 15% saturated picric acid dissolved in 0.1 M phosphate buffer (PB; pH 7.3). The brains were then removed and stored in the fixative solution overnight. Sixty- or eighty-micrometer-thick coronal sections were cut on a Vibratome and processed according to a electron microscopic protocol (EM; Pyapali et al., 1998b). Sections were washed several times in 0.1 M PB, immersed in cryoprotective solution (25% sucrose, 10% glycerol in 0.01 M PB), freeze–thawed in liquid nitrogen, and washed again in several changes of 0.1 M PB before being incubated in ABC solution (2 hours to overnight). They were treated with 1% OsO_4 for 1 hour, dehydrated in ethanol and propylene oxide, counterstained with uranyl-acetate, and embedded in Durcupan (Pyapali et al., 1998b).

Shrinkage correction of neurons labeled in vitro

Cells that were incomplete, showed a weak peroxidase reaction, or demonstrated clearly truncated dendritic branches were excluded, usually because of the obvious loss of a critical section with the processing. Shrinkage was estimated by microscopic measurements of the overall slice dimensions along the axis parallel to the cell body layer (X axis) and the axis perpendicular to the cell body layer (to the hippocampal fissure; Y axis) while still in the chamber and then after fixation and dehydration. The section thickness (in the septotemporal direction; Z axis) was noted before and after processing by measuring the focal depth of the tissue sections after mounting and the distance from the slide to the bottom of the coverslip. Approximately 11% shrinkage was observed in each of the X and Y axes, whereas there was considerable shrinkage in the Z axis because of dehydration after mounting (e.g., in the Z direction, a 100-μm-thick section averaged 25.4 μm after fixation and dehydration). The correction factors for this shrinkage were defined to be 1.11 in each of the X and Y axes and 4.0 in the Z axis (Pyapali and Turner, 1996; Pyapali et al., 1998b).

Shrinkage correction of neurons labeled in vivo

To assess the degree of shrinkage in the X and Y dimensions in vivo, four penetrations into the brain were made by a 100-μm-diameter tungsten microelectrode (2 × 2 mm in the lateral and anteroposterior directions) by using stereotaxic coordinates. The rat was then perfused, and the sections were treated as described above. The middle of the tracks at the same depth in the hippocampus was determined, and the distances were measured. Before histological processing, the brain shrank 10% in all directions. After histologic processing, an additional 10% shrinkage was observed in the each axis. Overall, a 20% total shrinkage was assumed in each axis. The correction factor to correct for this shrinkage applied to all dimensions was 1.25.

Selection and reconstruction of labeled neurons

Complete and optimally labeled CA1 and CA3 pyramidal neurons and dentate granule (DG) cells fulfilled the initial requirements that processes should extend to the hippocampal fissure, and dendrites were sufficiently densely labeled so that all visible processes, including dendritic spines, could be followed at high magnification. Only a single cell was filled in a hemisphere or a slice. Neuronal processes were reconstructed across all sections containing processes by using a 100× oil-immersion lens (numerical aperture = 1.25) and a computer-based neuronal reconstruction system that included an automated stage and high-resolution monitor viewed through the

microscope drawing tube (Neurolucida; Microbrightfield). This system allowed accurate tracing of the cell processes in all three dimensions and the frequent verification and recording of dendritic diameters with a circular cursor. Each field of processes was traced with a bitpad cursor while viewing the cell and the computer monitor simultaneously; branches were followed sequentially, one microscope field at a time. Focusing to maintain processes in clear view was performed with a joystick controller, and these changes in the depth were continuously recorded by the computer program, together with the X–Y location. Dendritic branches that continued into the next section were marked as "incomplete endings." The adjacent section was then superimposed over the computer overlay viewed on the monitor (the tracing of the previous section), and the incomplete dendritic branches were aligned with appropriate processes in this new section and the tracing was continued. The full digitized representation of the neuron in three dimensions could be viewed or edited to ensure accuracy.

TABLE 1. Measures of Dendritic Morphology[1]

$\lvert$branch order$\rvert$	1	Maximal branch order
$\langle$terminal order$\rangle$	1	Average branch order of terminals
N_{bp}	1	Total number of branch points (or terminals)
V, L, A		Total volume, length, area
$\lvert D_p \rvert$		Maximum terminal path distance from the soma
$\lvert D_s \rvert$		Maximum terminal straight line distance from the soma
$\langle D_{p,term} \rangle$, $\langle D_{s,term} \rangle$		Average path and straight line distances of terminals
$\langle R_d/R_p \rangle$		Mean radius ratio of daughter to parent branches
Apical–basal asymmetry	3	Asymmetry of apical and, where present, basal arborizations
Asymmetric ratio	3	Ratio of apical to basal asymmetries, if defined
Weighted asymmetry	5	Mean asymmetry weighted by branch order
vm_1, etc.		Moments of the mass distribution about the principal axes
Asphericity		Ratio of the smallest to largest moments
$C_{m,x}$, $C_{m,y}$		Center of mass along and perpendicular to the principal axis
$\sigma_{m,x}$, $\sigma_{m,y}$		As above, for the standard deviation
$Fractal_\alpha$, $fractal_\beta$	7	Parameters in the least squares fit to the "fractal" scaling relation
$F_{s-t,\omega}$, $F_{t-s,\omega}$	14	Average soma–terminal and terminal–soma attenuation at angular frequency ω

[1]Summary of all the scalar valued measures employed, corresponding to the data in Table 2 and Figure 1.

DENDRITIC ANALYSIS METHODS

Branching measures

The structure may be expressed as a set of points p. With each point there is associated a radius r(p), three coordinates x(p), y(p), and z(p), and a set of neighboring ("sibling") points $\mathbb{S}(p)$ to which p is connected. It is convenient to define one of the points p* as being the center of the structure, biologically in the soma, and defined here conveniently as the point of maximal radius. The parent P(p) of point p can then be defined as the element of $\mathbb{S}(p)$ on a direct line between p and p* and of its daughters $\mathbb{D}(p)$ as the rest of the elements of $\mathbb{S}(p)$.

A number of quantities may be defined with no reference to the positions of the points. In particular, the branch order B(p) can be defined by:

$$B(p^*) = 0$$

$$B(q),\ q \in \mathbb{D}(p) = \begin{cases} B(p) & \text{if } N(D(p)) = 1 \\ B(p) + 1 & \text{otherwise} \end{cases} \tag{1}$$

where the operator $N(\mathbb{S})$ gives the number of elements in the set $\mathbb{S}$. The number of terminals T(p) downstream of p satisfies

$$T(p) = \sum_{q \in \mathbb{D}(p)} T(q) \tag{2}$$

and the asymmetry A(p) is given by

$$A(p) = \begin{cases} 0 & \text{if } t_1 = t_2 \\ t_1 - t_2/(t_1 + t_2 - 2) & \text{if } t_1 \neq t_2 \end{cases} \tag{3}$$

where $t_1 = T(d_1)$, $t_2 = T(d_2)$, and d_1 and d_2 are the two elements of D(P(p)) in the case that it has two elements. For more than two daughters, the asymmetry ratio is undefined. The mean asymmetry is then

$$A_0 = \frac{1}{T(p^*)} \sum_{p \in \mathbb{B}} A(p) \tag{4}$$

where $\mathbb{B}$ is the set of branch points. A weighted mean of A(p) serves to quantify the variation of asymmetry with branch order

$$A_1 = \frac{\sum_{p \in \mathbb{B}} A(p)\, B(p)}{\sum_{p \in \mathbb{B}} B(p)}. \tag{5}$$

A number of other quantities used in the morphological analysis defined in terms only of B(p), T(p) and A(p) are listed in Table 1.

"Fractal" dimension

The fractal properties of neurons were assessed by the calliper method, which consists of measuring the apparent length $L(\lambda)$ when the structure is viewed at various resolutions, defined as different values for λ for the shortest resolvable section. In practice, this amounts to measuring off sections as if with callipers and ignoring features smaller than λ. Although normally only applied to curves, the extension to branching structures can easily be made by cutting off the minor branch at each branch point and treating it as the beginning of a separate tree. For a fractal, these quantities show a power law relation

$$L(\lambda) \propto \lambda^{1-f} \tag{6}$$

where the quantity f in the exponent is termed the fractal dimension. As illustrated in the discussion, this is not the case for the neurons considered here. They do, however, follow a relation of the form

$$\log L = \log L_0 - \exp(\alpha(\log \lambda - \beta)). \tag{7}$$

The quantities α and β were found by least squares fitting.

Electrotonic properties

To calculate passive electrical properties from the morphology of a neuron, it is necessary to know the specific cytoplasmic resistivity R_i, the membrane resistance R_m, and capacitance C_m. Following Spruston et al. (1994), the

values $R_m = 30\ K\Omega cm^2$, $C_m = 1\ \mu F cm^{-2}$, and $R_i = 200\ \Omega cm$ are used throughout.

Given the structure as defined from the database, the frequency-dependent admittance (Carnevale et al., 1997; Turner, 1984a; Zador et al., 1995) of the arborization beginning at p with p, q as its first section, $q \in \mathbb{S}(p)$, is

$$Y(p, q) = \frac{\pi(r(p) + r(q))^{3/2} q}{2\sqrt{R_m R_i}} \frac{\sinh(\xi X) + Y_t \cosh(\xi X)}{\cosh(\xi X) + Y_t \sinh(\xi X)} \quad (8)$$

with

$$X = 2l \sqrt{\frac{R_i}{(r(p) + r(q))\, R_m}}, \quad (9)$$

$$\xi = \sqrt{1 + i\omega}, \quad (10)$$

and

$$Y_t = \sum_{s \in \mathbb{D}(q), s \neq p} Y(q, s), \quad (11)$$

where ω is the angular frequency for the signal and l is the length of the section p − q. The attenuation if an alternating potential of angular frequency ω over the section p, q is then

$$\nabla(p, q, \omega) = |\cosh(qX) + Y_t \sinh(qX)|^{-1}. \quad (12)$$

Having evaluated all the attenuations, two quantities can be defined on the structure that captures most of the commonly used measures of passive electrotonic properties: the centripetal and centrifugal attenuations at frequency ω, ∇_{cp}, and ∇_{cf}. In terms of the single segment attenuation,

$$\nabla_{cp,\omega}(p) = \begin{cases} 1 & \text{if } p = p^* \\ \nabla_{cp,\omega}(P(p))\, \nabla(p, P(p), \omega) & \text{otherwise} \end{cases}$$

$$\nabla_{cf,\omega}(p) = \begin{cases} 1 & \text{if } p = p^* \\ \nabla_{cf,\omega}(P(p))\, \nabla(P(p), p, \omega) & \text{otherwise.} \end{cases} \quad (13)$$

These quantities have been extensively described and illustrated elsewhere (Carnevale et al., 1997; Henze et al., 1996; Mainen et al., 1996; Major et al., 1994; Spruston et al., 1994; Turner, 1984a,b; Turner et al., 1991; Zador et al., 1995). Many of the useful whole-cell measures arise from the combination of attenuation with the branch distribution, as described below, but the topology alone allows construction of, for example, the mean soma to terminal attenuation,

$$F_{s-t,\omega} = \frac{1}{T(p^*)} \sum_{p \in \mathbb{T}} \nabla_{cp,\omega}(p) \quad (14)$$

where $\mathbb{T}$ is the set of terminal points. This attenuation measure and the corresponding quantity for the attenuation of sinusoidal potentials applied at the terminals and measured at the soma are both functions of the angular frequency ω. For the analysis, these functions are sampled at two points, $\omega = 10$ and $\omega = 1000$, corresponding to frequencies of about 1.6 and 160 Hz.

Branch distribution

The spatial distribution of branches is computed with the aid of a cumulative weighting function W(p), defined in terms of a local weight w(p) by

$$W(p) = w(p) + \sum_{q \in \mathbb{D}(p)} W(d), \quad (15)$$

the mean direction of an arborization can then be expressed as

$$X(p) = \sum_{d \in \mathbb{D}(p)} W(d)\, X(d) + w(p)\, V(p, d) \quad (16)$$

where V(p, d) is the vector from p to d. For a neuron having opposing apical and basal dendrites, the main axis can be computed by as a vector sum of the mean directions of the arborizations at the soma, in which the signs of the components are selected to maximize the modulus of the sum. Natural choices for the weighting W(p) are the length and the volume of the section from P(p) to p. The segment length is used in the present calculations.

RESULTS

The nontrivial single valued measures employed are summarized in Table 1, and their distributions for the main cell types in the sample are shown in Figure 1. The cells are grouped as granule cells, interneurons, CA3 pyramidal cells, and CA1 pyramidal cells. Aged neurons, those subject to kainic acid lesions, and minor cell groups ($\leq$10 cells per group) present in the original dataset (Cannon et al., 1998) have been excluded. The average properties of the various groups are shown in Table 2 with the results of an analysis of variance (ANOVA) test for significant difference in the mean. Although there is considerable overlap between types, the ANOVA test indicates that for all measures the populations are nevertheless not identical.

Perhaps the most direct message from Figure 1 and Table 2 is that most of the measures show a broad spread for each cell type, with a substantial overlap between types. Parameters with less overlap between cell classes are the simpler ones: for example, all the pyramidal cells have more branch points than the most densely branching granule cells or interneurons, and all the cells with maximal branch orders in excess of 10 are pyramidal. CA1 and CA3 pyramidal cells separate to some extent in that the upper half of the branch order scale (20–40) is populated exclusively by CA1 cells, although there remains some overlap with CA3 cells in the range 10–20. The granule cells and interneurons are partly separated by the latter having in general a lower volume-to-area ratio and also a greater mean soma-to-terminal attenuation. It should be noted that the attenuation scale is logarithmic, so the only cells that can be described as electrically compact are the interneurons. Indeed, the soma-to-terminal attenuation at $\omega = 100$ shows no overlap at all between the interneurons and either the CA1 pyramidal cells or the granule cells.

The results of pairwise Kolmogorov–Smirnov (K-S) test on the four main cell groupings are shown in the right-

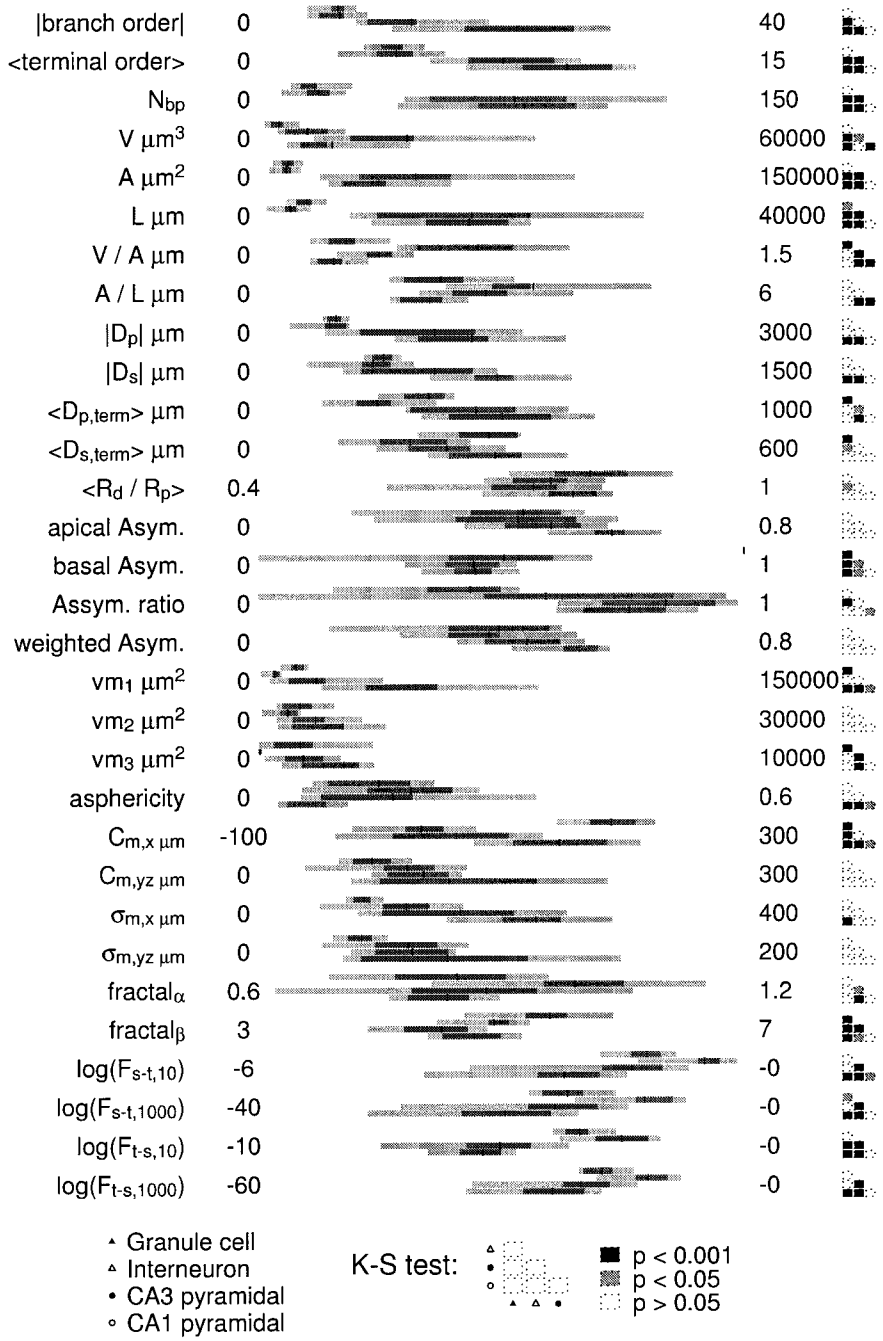

Fig. 1. Raw measurement data grouped according to cell type: granule cells, interneurons, CA3 pyramidal cells, and CA1 pyramidal cells. For each quantity there are four bars for these cell types in that order, from the top. The shading shows the variation of each measure in the population. Light shading covers the area between the 5 and 95 percentiles; darker shading shows the 25–75% range, and the vertical bar shows the mean of the data. All the scales are linear. For each quantity the lower and upper limits are shown at the left and right, respectively. The four groups of cells give rise to six distinct pairs of groups. The results of the Kolmogorov–Smirnov (K-S) test for each pairs are shown at the far right (see the key at the bottom for pair labeling). For each pair the shading indicates the probability P that the two groups came from the same population; small p indicates a significant difference in the distributions.

hand column of Figure 1. This test, which uses only the relative ordering of the points and therefore is scale independent, indicates the likelihood of finding two such samples from the same underlying distribution. Small probabilities (darker shading in the figure) indicate greater differences between the groups. From these data it can be seen that the most discriminative measures—those with the most pairwise tests significant at the 1% level—are the number of branch points, total length and area, and the electrotonic attenuation, which are in effect only different ways of quantifying the size of the structure. The second term in the fit of the scaling properties, analogous to the

TABLE 2. Mean Morphologic Properties by Cell Type[1]

	CA1 pyramidal in vivo	CA3 pyramidal in vivo	Granule cell in vivo	Interneuron in vitro	
Type	Young	Young	Young	Young	
n cells	23	15	19	13	
$\lvert$branch order$\rvert$	21.7 ± 5.9	12.9 ± 3.7	6.53 ± 1.2	6.69 ± 1.8	**
⟨terminal order⟩	9.64 ± 1.8	7.69 ± 1.5	4.34 ± 0.59	4.25 ± 0.97	**
N_{bp}	82.7 ± 22	80.5 ± 28	17.3 ± 5.4	18.5 ± 6	**
V (μm^3)	8700 ± 6300	19100 ± 10000	2540 ± 1200	6080 ± 3300	**
A (μm^2)	36100 ± 17000	50400 ± 24000	9010 ± 2800	8620 ± 2900	**
L (μm)	17400 ± 6200	18100 ± 8600	4000 ± 940	2660 ± 960	**
V/A (μm)	0.229 ± 0.059	0.375 ± 0.067	0.271 ± 0.073	0.678 ± 0.19	**
A/L (μm)	2.06 ± 0.46	2.85 ± 0.55	2.25 ± 0.52	3.4 ± 0.76	**
$\lvert D_p \rvert$ (μm)	1330 ± 450	1120 ± 460	479 ± 54	440 ± 110	**
$\lvert D_s \rvert$ (μm)	746 ± 140	561 ± 150	386 ± 38	354 ± 95	**
$\langle D_{p,term} \rangle$ (μm)	504 ± 150	457 ± 130	351 ± 46	245 ± 70	**
$\langle D_{s,term} \rangle$ (μm)	294 ± 66	238 ± 48	285 ± 39	187 ± 60	**
$\langle R_d/R_p \rangle$	0.787 ± 0.053	0.74 ± 0.084	0.81 ± 0.065	0.761 ± 0.045	*
Apical asymmetry	0.588 ± 0.048	0.489 ± 0.075	0.436 ± 0.1	0.427 ± 0.15	**
Basal asymmetry	0.444 ± 0.069	0.44 ± 0.079	±	0.506 ± 0.19	**
Asymmetric ratio	0.758 ± 0.11	0.842 ± 0.12	0.436 ± 0.1	0.592 ± 0.27	**
Weighted asymmetry	0.533 ± 0.058	0.446 ± 0.071	0.397 ± 0.11	0.38 ± 0.1	**
vm_1 (μm^2)	49000 ± 23000	18800 ± 10000	11600 ± 2400	5030 ± 1800	**
vm_2 (μm^2)	5150 ± 5800	3700 ± 1700	2580 ± 1200	1810 ± 870	*
vm_3 (μm^2)	1780 ± 1400	964 ± 480	859 ± 680	38 ± 32	**
Asphericity	0.0691 ± 0.043	0.163 ± 0.11	0.149 ± 0.065	0.189 ± 0.081	**
$C_{m,x}$ (μm)	150 ± 48	67 ± 57	191 ± 24	33.8 ± 35	**
$C_{m,yz}$ (μm)	118 ± 60	104 ± 23	70 ± 14	91.8 ± 28	*
$\sigma_{m,x}$ (μm)	230 ± 45	171 ± 57	87 ± 8.9	122 ± 50	**
σ_m, yz (μm)	78.2 ± 42	65.1 ± 19	42.5 ± 7.2	61.8 ± 17	*
$Fractal_\alpha$	0.833 ± 0.045	0.885 ± 0.12	0.846 ± 0.092	0.991 ± 0.11	**
$Fractal_\beta$	4.78 ± 0.27	4.53 ± 0.32	5.4 ± 0.35	4.94 ± 0.26	**
$Log(F_{s-t,10})$	−2.25 ± 0.72	−1.43 ± 0.68	−1.2 ± 0.25	−0.488 ± 0.36	**
$Log(F_{s-t,1,000})$	−19.9 ± 5.6	−15.9 ± 4.9	−14.6 ± 2.1	−8.21 ± 3	**
$Log(F_{t-s,10})$	−5.41 ± 0.71	−5.08 ± 0.97	−3.39 ± 0.35	−2.52 ± 0.78	**
$Log(F_{t-s,1,000})$	−23.9 ± 5.7	−20.4 ± 5.3	−17.6 ± 2.1	−11.9 ± 3.4	**

[1]Mean topologic, morpholigic, and electrical properties of the four main cell groups. Values shown are the mean ± standard deviation. The last column shows the results of an analysis of variance test for significant difference in the mean among the four groups, showing significance at the 5% (*) and 0.1% (**) levels, against the null hypothesis that they are four random samples from the same population. The quantities used are summarized in Table 1.

fractal dimension, also shows significant differences between the main cell types. It is related to the size of the structure in that from equation 7 it sets the length scale at which the scaling relation changes slope.

Eight of the measures which show the greatest separation between these four cell types are plotted pairwise in the first four panels of Figure 2, although no significance is attached to the choice of pairs. The standard deviation of the mass moment along the principal axis, $\sigma_{m,x}$ is included mainly for its clear separation of the granule cells when plotted against the center of mass along that axis. From Figure 2 it is clear that the interneurons and granule cells separate readily from each other and from the pyramidal cells. Only in the maximum branch order and soma–terminal attenuation do the CA1 and CA3 populations separate appreciably, and even then there remains a considerable overlap.

Although no single measure reliably discriminates between the CA1 and CA3 pyramidal cells, it is conceivable that some linear combination of the scalar measures may do so. One approach to finding such combinations is principal components analysis. Given a population of m objects and measures $x_{i,j}$ for the ith measure evaluated on object j, the covariance matrix,

$$C_{i,j} = \frac{1}{m} \sum_k x_{i,k} x_{j,k}, \tag{17}$$

indicates how the measures interrelate across the population. Uncorrelated measures give zero entries in the matrix, whereas highly correlated or anticorrelated measures show large positive or negative covariances. The matrix can be transformed into a space in which the covariances of any measure with any other except itself is zero by mapping it onto its eigenvectors. All the eigenvalues and the first four eigenvectors are shown in Figure 3.

Figure 2E, F shows the positions of the cells on the first three principal components. They show a separation of the main cell types comparable to, but not substantially better than, the best individual measures. This suggests that not much more can be gained from the single valued statistics than is already present in the direct comparisons of the raw data. The fourth and higher order principal components show no significant correlation with cell type.

Vector measures

The foregoing analysis has focused on single quantities that may be derived to summarize some feature of the dendritic arborization. Although many of these quantities do show consistent difference between cell types, they are necessarily rather coarse measures. This averaging process may lose important characteristics of different cell types that relate to the variation of some quantity within the structure. The next level of detail concerns vector valued quantities, which may be expressed as a function of position in the dendritic tree, where the latter could be taken as the branch order, distance from the soma along the structure, the true spatial location, or any of a number of other functions. Clearly there are far too many possibilities for an exhaustive examination. Instead, attention is restricted to two hypotheses concerning the relation of the probability of branching with distance from the soma and with the age of the cell. Van Pelt (1997) suggested that segment length may increase as a function of distance from the soma and, conversely, that the probability of branching may decrease. This hypothesis suggests that in the more distal dendritic areas there are somewhat longer branches and fewer branch points. Pyapali and Turner

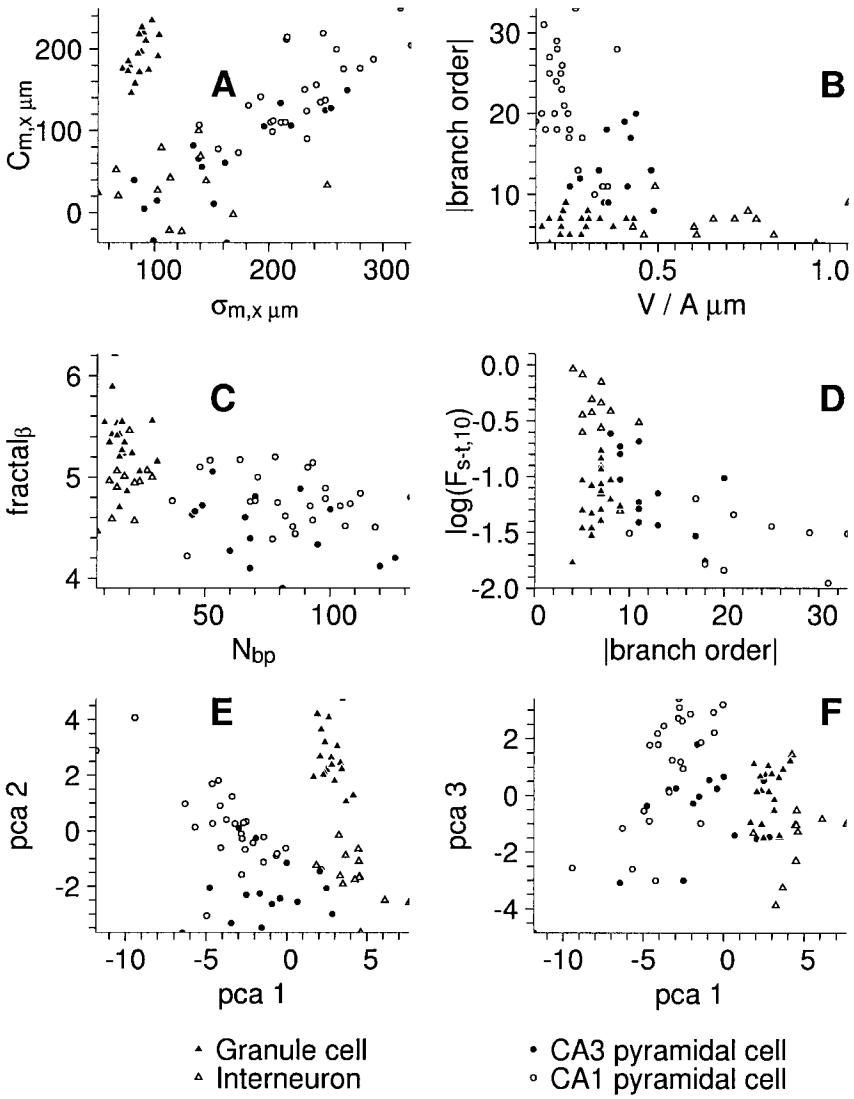

Fig. 2. **A–F:** The most discriminative measures for the four main cell types: granule cells, interneurons, CA1 pyramidal, cells and CA3 pyramidal cells. The measures have been plotted pairwise for clarity, but no significance is attached to the particular choice of pairings. E and F show the second and third principal components, respectively, against the first principal component.

(1996) found increased branching with aging, suggestive of dendritic sprouting.

Branching probability

Figure 4 shows the variation of mean distance from the soma with branch point order for representative cells from each group. For those cells that have a clear apical–basal separation, two relations are shown. The graphs show the mean somatic distance D(n) for all branch points of order n in the structure. In most cases D(n) increases with n, although exceptions are possible, as when a cell has some long branches of low order and short bushy branches. The mean distance will be high for the terminal points of the long branches but lower for points of higher order, when the long ones no longer enter the average. For most cases, the relation is almost linear, with a slight upward curvature, and D(n) can be well represented as a quadratic in n. Because D(n) measures the average distance along the structure to a branch point of order n, its reciprocal gives the rate of increase of branch order with distance, which is also the branching probability per unit length:

$$P_{br} = \frac{dn}{dD} = \left(\frac{dD}{dn}\right)^{-1}. \quad (18)$$

Thus, the branching probability is inversely related to the slope of the D(n) curve. An upward curve on D(n) corresponds to a decreasing branching probability with branch order. The slope dD/dn for apical and basal arborizations for all the CA1 an CA3 cells are shown in Figure 4B. The slope and curvature d^2D/dn^2 are shown for all cells in Figure 4C.

No significant correlation is apparent between the apical and basal gradients, but there is a tendency for the second derivative to be positive for the apical arborizations.

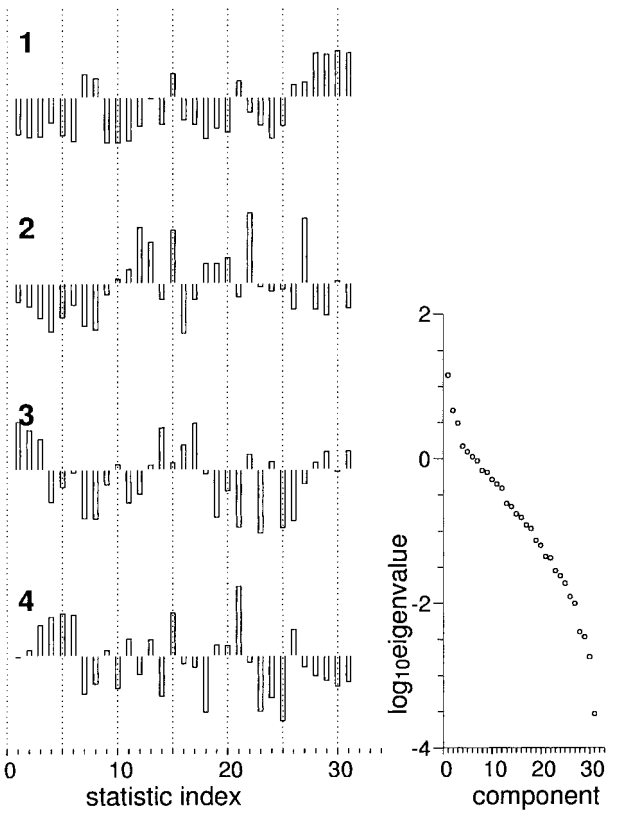

Fig. 3. Principal components of the raw data presented in Figure 1. All the eigenvalues of the covariance matrix are shown on the right, with the first four principal components (1–4). Each principal component is a vector representing a linear combination of the raw measures. The elements of the vectors are shown as bars, where the nth bar corresponds to the nth measure as ordered in Figure 1 and Table 2. The first three eigenvalues are above the trend of the remainder and represent significant components of the data.

Because of their lower branch orders, the data are too noisy for basal arborizations to give a reliable curvature. The tendency to positive ν_{apical} supports the suggestion of Uemura et al. (1995) that the main departure from a uniform branching probability necessary to match real neurons is that the branching probability should fall slightly with increasing branch order.

Age dependence

It has been suggested (Woldenberg et al., 1993) that the structure of young neurons is consistent with relatively simple growth rules, such as a uniform branching probability, whereas aged neurons have been modified more by their environment and therefore deviate from such growth rules. The present sample contains 11 young CA1 pyramidal cells. The main archive also contains 15 cells from animals 22–24 months old that were studied and labeled in vitro, having undergone behavioral testing.

The differences between these populations for selected measures are shown in Figure 5 in the same style as that in Figure 1. The upper lines indicate aged cells, the lower ones the young cells. The only measure that is significantly different on a K-S test at 0.1% is the mean straight line distance from the soma to the terminals, $\langle D_{s,term} \rangle$, which is significantly greater for the aged cells. At the 5% level, the second parameter of the fractal fit is also significant.

The first and second derivatives of the path length–branch order relation for these neurons are shown in Figure 6. None of these distributions is significantly different on a K-S test between the young and aged neurons. The relative difference between the path distance and straight line distance to terminals can be better seen in Figure 6C,D, which shows the ration d_s/d_p for all branch points in the structures. All values must be less than one, but the aged neurons show a significant population of points between 0.7 and 1 that are almost completely absent, except for points fairly near the soma, in the young neurons. Thus, the paths between the soma and dendrites have become less convoluted because of age-related dendritic remodeling.

DISCUSSION

Topologic, scaling, and electrotonic analyses show that multiple parameters relating to structural complexity and branching patterns can differentiate neurons, by using the dendritic structure, into the major classes of hippocampal neurons, which are recognized from neuroanatomy. Although some measures show a stronger prediction for this class separation than others, all of the parameters we present appear to be important in understanding morphologic and functional differences between these different cell types. These parameters may also be helpful in understanding dendritic developmental principles and functional alterations with lesions and senescence.

Measurement of dendritic structures

Many statistics have been employed in studies of dendritic structure with a view to classifying neurons on morphologic criteria and to deriving rules that are obeyed during their development (Henze et al., 1996; Ishizuka et al., 1995; Uylings et al., 1986; Van Pelt et al., 1997). Some of these, such as Sholl (1953) branching analysis, are primarily of interest for image data where a fully connected branching structure has not been extracted. Because a two-dimensional image can easily be constructed from a three-dimensional structure, no methods derived specifically for image data were employed in the present study. Anything that can be measured with a two-dimensional projection and subsequent pixelation can presumably be measured more cleanly and reliably from the original three-dimensional data. For this reason, all the measures employed here are defined directly on three-dimensional structures. It is important, however, to construct a sufficient breadth of statistics on such structures to ensure capturing a superset of the information available from image-based methods that have already demonstrated their worth as statistics for morphologic classification.

"Fractal" dimension

Several researchers have addressed the problem of computing the fractal dimension of a neuron from image data alone (Caserta et al., 1995; Jelinek and Fernandez, 1998; Smith et al., 1996). Although three-dimensional image stacks from confocal microscopy have the advantage of being free from any artifacts of the tracing process, it is often unclear exactly how the structure is connected. In the case of two-dimensional image data, there is the other problem of a failure to distinguish branchings from coincidental crossings and superimposition when no connection

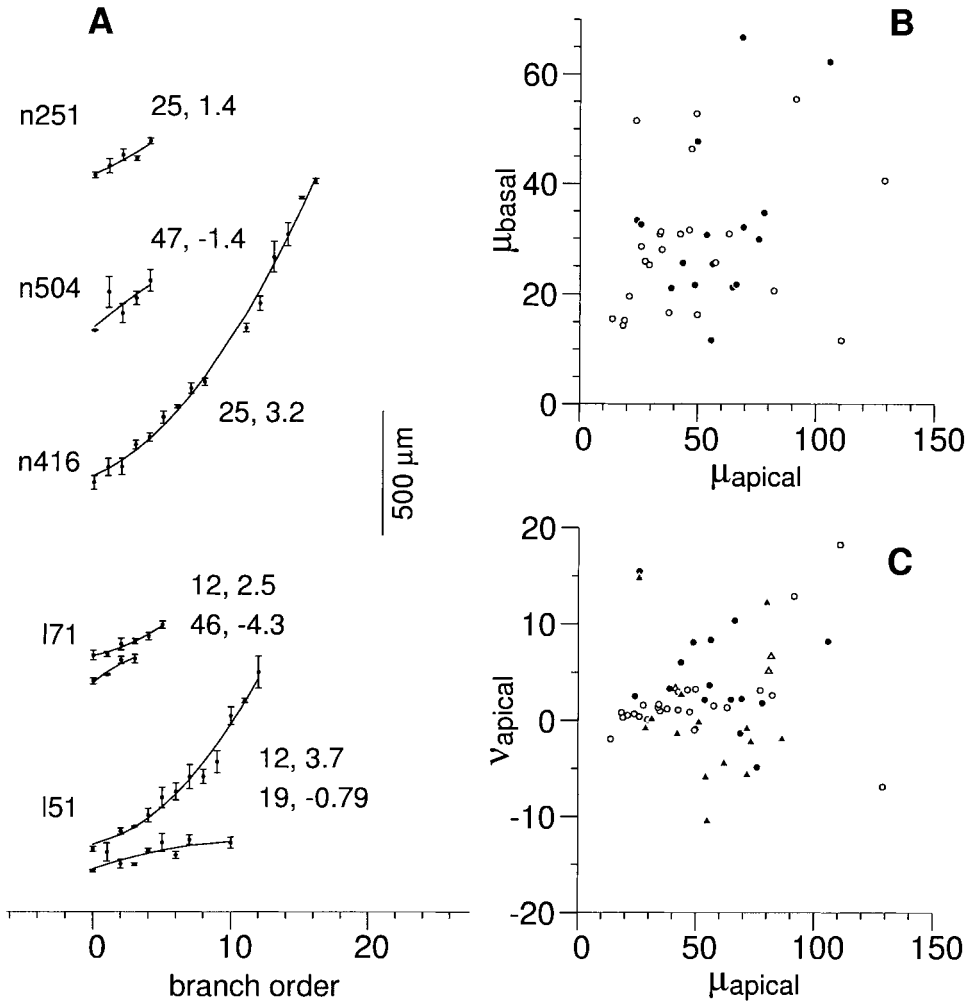

Fig. 4. The relation between distance from the soma and branch order for branch points. **A:** Example relations for the same six representative neurons. For each branch order, the mean ± standard deviation of its distance from the soma is shown separately for apical and, if present, basal dendrites. The means are fitted by a quadratic function $d = \mu x + \nu x^2$ for the distance d in terms of the branch order x. Each example fit is labeled with the corresponding µ and ν. **B:** Slopes of the distance–branch order relation for apical and basal arborizations of CA1 (open circles) and CA3 (filled circles) pyramidal cells. **C:** Slope µ and curvature ν of the apical arborizations of all cells grouped according to the main types: CA1 and CA3 pyramidal cells as in C, granule cells (filled triangles) and interneurons (open triangles).

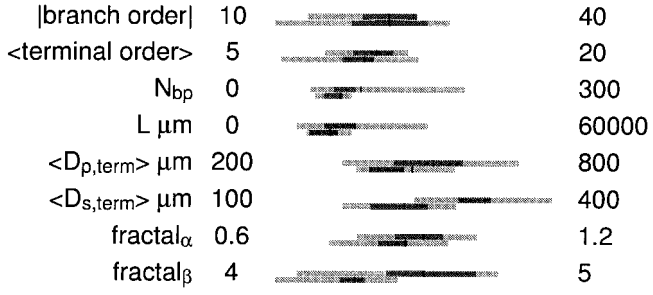

Fig. 5. Raw measurement data for selected parameters for aged (upper lines) and young (lower lines) CA1 pyramidal neurons. The symbols and shading are the same as those in Figure 1.

actually exists. Although algorithms have been presented to extract a value for the "fractal dimension" from an image of a cell, it is often not clear how this value relates to the conventional understanding of fractal dimension (Jelinek and Fernandez, 1998; Smith et al., 1996). Availability of the full three-dimensional structure makes more conventional methods accessible for studying fractal properties. The calliper method used for measuring fractal dimension is illustrated in Figure 7 for a real neuron and for two partial fractals generated by a simple recurrence stopping when the new sections would be less than some lower limit, set at 1.0 µm in Figure 7, where the fractals are scaled to be the same size as the neuron.

Both partial fractals show a linear relation in log L against log λ, spanning almost two orders of magnitude. The neuron, however, shows a continuous variation of gradient in the log–log plot, with no characteristic slope, and hence it does not, properly speaking, have a single fractal dimension. This result is similar to the neuronal examples shown in Smith et al. (1996; Fig. 7), although in that report the resolution is lower and a straight line is put through the points in spite of the apparent curve. The flattening of the relation at small scales is due to the limited resolution of the data with light microscopic recon-

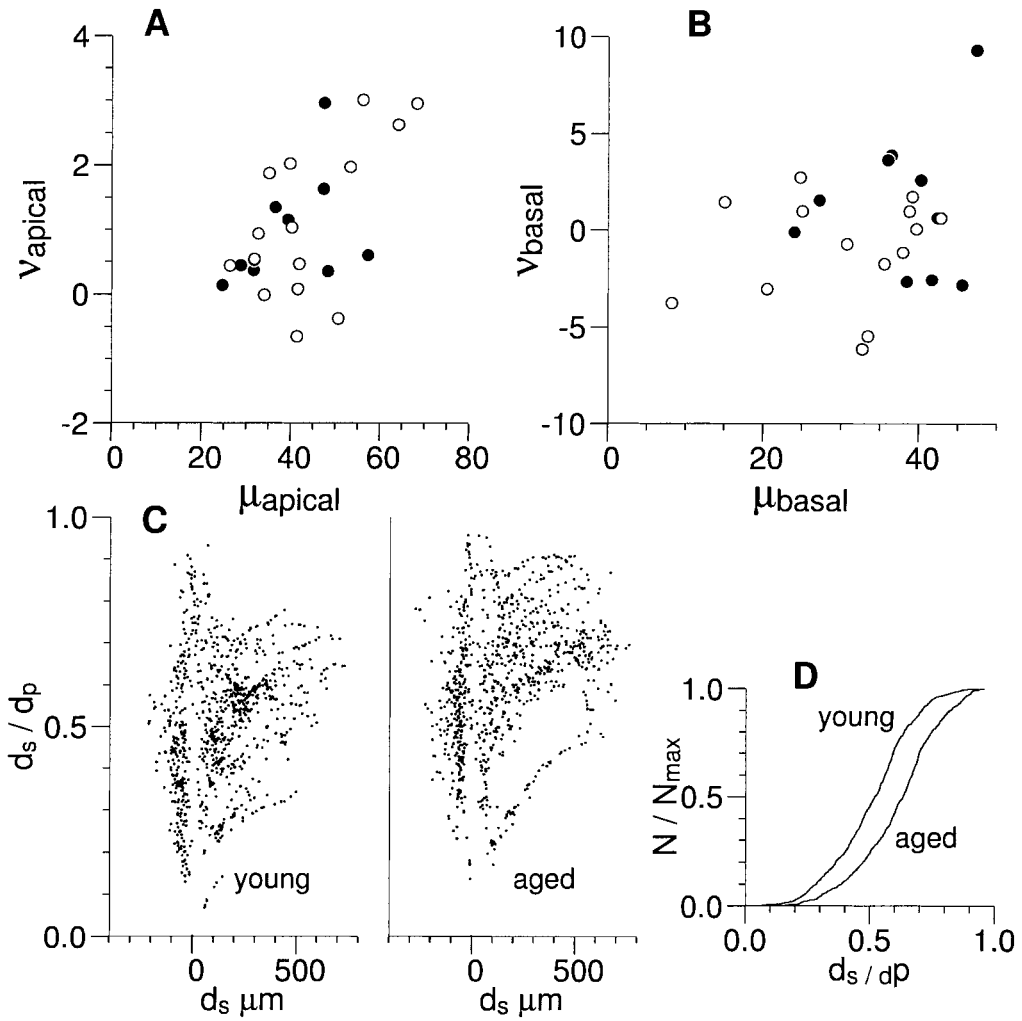

Fig. 6. Branch distribution of young and aged CA1 pyramidal cells. **A:** Slope and curvature of the apical distance–branch order relation. Most cells show a positive curvature, indicating a decreasing branching probability, but there are no significant differences between the two sets. **B:** As in A but for the basal dendrites. The difference between the two populations is not significant. **C:** Straightness index, d_s/d_p against d_s, for young (left) and aged (right) cells, where d_s is the straight line distance of a point from the soma and d_p is its distance measured along the neuron. The quantity d_s/d_p is always less than one. Values nearer one indicate that the paths are closer to being straight lines. Paths in the aged cells are significantly straighter, as indicated by the cumulative distributions (**D**), which differ by the Kolmogorov-Smirnoff test at the 1% level.

structions and to the steepening at large scales to the finite size of the structure. Comparison with the partial fractals in Figure 7 shows that even between these limits the structure is more subtle than a fractal. The nonlinearity of the log λ–log L relation does not, however, mean that the calculation is useless: indeed it has rather more information than would be the case if it were a simple power law. The next simplest functional form to try as a representation of this curve should have two parameters. Examination of curves for a number of neurons suggests the two-parameter fit given in equation 7. Least squares fits of α and β for five typical neurons covering the main cell types studied are shown in Figure 8.

In a few cases, such as cell l51 at the top of Figure 8, there is a fairly straight section of the scaling relation. In this case, it extends for almost two e-foldings centered on a scale of about 20 μm. This is also one of the most complex structures considered, suggesting that in a few cases a conventional fractal dimension may be appropriate for the range 10–100 μm. However, because the large majority of the cells shows a much better fit to equation 7, the two fitted quantities α and β have been used throughout to characterize the scaling relation.

Electrotonic properties

In the attenuation calculations, only one set of values for the specific cytoplasmic resistivity R_i and the membrane resistance R_m have been used. However, there is some evidence that these quantities vary consistently between groups of neurons, but it would be useless to employ different values in this analysis according to neuronal type and then try to relate the results back to the very classification that was assumed in the first place. Clearly, electrical properties such as membrane resistance and, even more so, channel populations are very powerful discriminators of neuronal type, but they lie beyond the

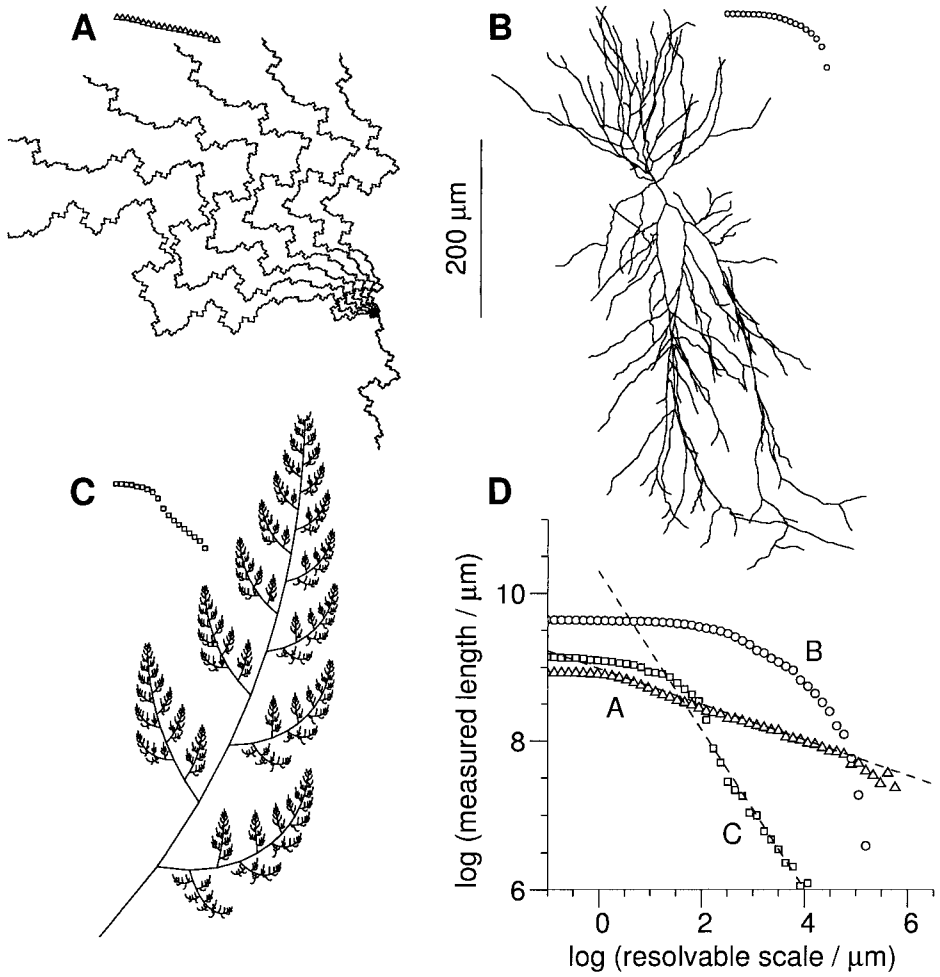

Fig. 7. "Fractal" dimensions of two partial fractals and a neuron. The partial fractals (**A,C**) generated by a recurrence relation show a linear relation in the log (measured length) against log (resolvable scale) plot (**D**), whereas there is no linear section for the neuron (**B**). The length shown for a particular resolvable scale (abscissa in D) is as would be measured with callipers of that separation. Below the physically imposed resolution of the data, all the curves flatten off because there is no more structure to be seen by reexamining it at a smaller scale.

scope of the current study, which focuses on the use of morphology for classifying neurons. Although there is no simple relation connecting resistances with the derived attenuations, the nonlinearities are small. Changes in R_m and R_i over plausible ranges change the magnitudes of the attenuation but not the relative ordering of cells by their electrical compactness. Changing their values up or down by a factor of two produces results very little different from that of the last four rows in Figure 1 and leave the conclusions about the statistical separation of cell types unchanged.

Class separation among hippocampal neurons

There are large differences between the cell types we have studied, generally following the differentiation of traditional hippocampal cell classes. The characteristic differences include particularly branch order, polarity and center of mass, and one of the fractal or scaling parameters, suggesting a large difference in dendritic complexity among the different classes. Pyramidal cells can be differentiated on several grounds from dentate granule cells and from interneurons. In almost all the individual measures employed, the different cell groups show statistically distinct means but a considerable overlap of the population. The overlap is particularly large for the smaller differences between CA1 and CA3 pyramidal cells in most parameters, as compared with the other two smaller cell types. Interneurons are ectopic in comparison with the tightly clustered principal cell classes, so location may be very important for their multipolar differentiation. From this argument alone, however, the lack of basilar dendrites in granule cells may either be a function of location (and, hence, inhibition of growth of basilar dendrites by the hilus) or an intrinsic tendency of the cells to only grow in one direction, together with cues for pointing out the desired direction. Interestingly, the scaling between cells does not necessarily imply increased complexity because the much smaller CA1 pyramidal neurons, compared with the large CA3 pyramidal cells, show much more complex structure, particularly in levels of branch orders. Thus, various morphological parameters may show dissociation from functional and size estimates.

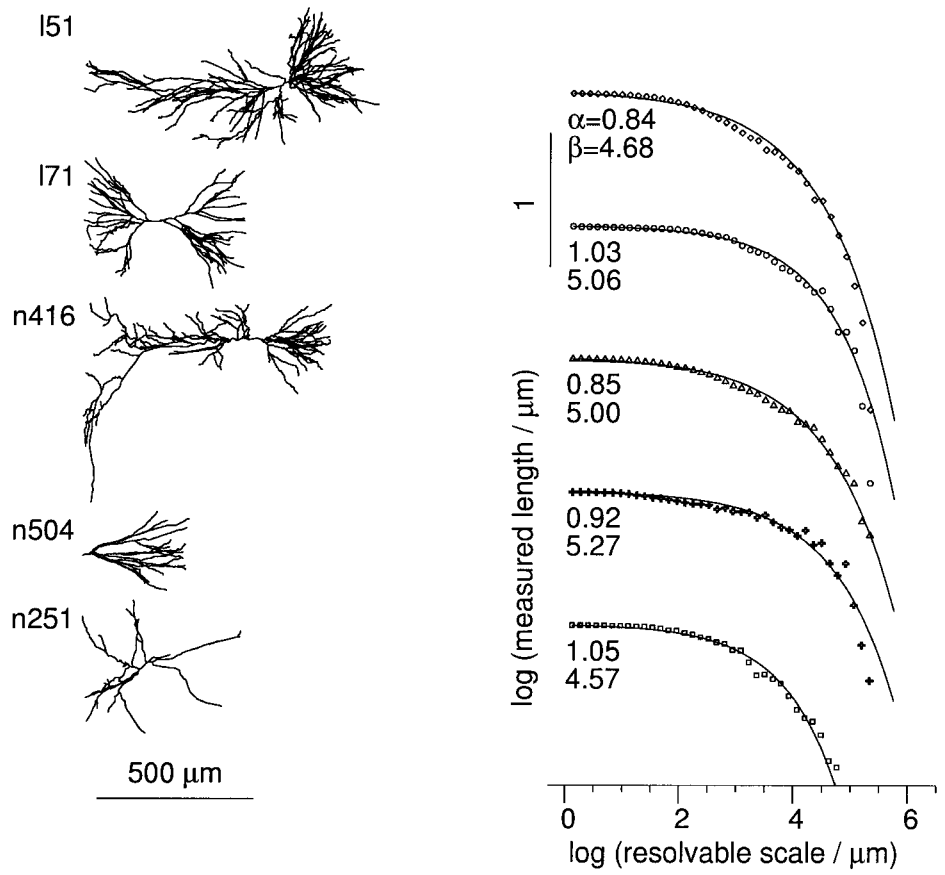

Fig. 8. Least squares fit to the length–scale relations for typical neurons of each of the main cell types. These are, from the top, large and small CA1 pyramidal cells, a CA3 pyramidal cell, a granule cell, and an interneuron. The scaling relation for each cell is shown alongside. The solid line is a least squares fit of the function $\log l(\lambda) = \log l(0) - \exp(\alpha(\log \lambda - \beta))$, where λ is the resolvable scale, and $l(\lambda)$ is the length measured at that resolution. The values of α and β are shown beside each line.

Dendritic growth models of hippocampal neurons

Clear differentiation of intrinsic and extrinsic growth factors that contribute to the mature dendritic appearance of hippocampal neurons is not possible from this type of analysis, but several other types of experiments have demonstrated some of these characteristics. For example, primary hippocampal tissue cultures, in which neurons are missing many of the external trophic and environmental constraints (or they are diffuse rather than focal due to the lack of extracellular tissue), show persistent pyramidal shapes, although they are somewhat more multipolar (Shetty et al., 1994; Uemura et al., 1995). Hippocampal stem cells also show some aspects of pyramidal neuronal shapes after partial differentiation with growth factors (Shetty and Turner, 1998), and neurons derived from ectopic fetal hippocampal grafts show much less oriented structure than in the organized hippocampus in vivo but remain pyramidal in many instances (Pyapali et al., 1994). Even though the soma is ectopic and in a naive environment, some branching characteristics are preserved, but much of the final dendritic configuration is shaped by the environment. This has been further confirmed in a study of granule cells deprived of innervation from entorhinal cortex, in which dendrites within the molecular layer fail to mature in the dentate gyrus (Zafirov et al., 1994). There are also mutants such as the reeler mutant (Stanfield and Cowan, 1979) that show a failure of dentate granule cells to migrate appropriately, with failure of a confined granule cell layer to form. It lacks *reelin* protein, which appears to function in multiple roles for neuronal migration and axon guidance (Alcantara et al., 1998).

These studies define in part the necessary conditions for normal dendritic maturation (Turner et al., 1998). First, migration to the appropriate cell layer appears critical because ectopic location may preclude normal afferent ingrowth. Proteins such as reelin may determine such appropriate migration in the hippocampus and neocortex (Alcantara et al., 1998), and neural grafts are inherently ectopic unless neuronal migration occurs in the grafted cell population (Pyapali et al., 1994; Shetty et al., 1994). After migration, inherent neuronal shape formation may occur, such as a bipolar or monopolar configuration, determined by anchoring provided by radial glia and larger cortical structures such as ventricles and pia. Second, normal ingrowth of afferents combined with appropriate receptivity of dendrites determines the extent of dendritic maturation. Thus, in the absence of important afferent fibers, dendrites may not mature in terms of complexity (Pyapali et al., 1994; Zafirov et al., 1994). This second stage suggests that activity-driven dendritic growth may be critical for full development of complex arborizations medi-

ated by both specific proteins and likely additional growth factors (Nedivi et al., 1998; Van Ooyen et al., 1983). In the mature neurons studied in the present report, we cannot differentiate the relative effects of these two influences.

Dendritic growth is further defined by the likelihood of branching as a function of either branch order or distance from the soma. As suggested by Van Pelt et al. (1997), there is a tendency for a decreasing probability of branching as a function of distance from the soma (Fig. 6). After dendritic maturation, neurons must constantly remodel in response to both routine and exceptional events. For example, after denervation dendrites must alter to accept new sprouting afferents, such as occurs in a kainic acid lesion resulting in denervation of CA1 pyramidal neurons (Pyapali and Turner, 1994). The robust dendritic sprouting response of CA1 pyramids to this lesion suggests a highly plastic state for this particular type of neuron. Likewise, during the lifespan of cortical neurons there is likely to be constant, dynamic remodeling, which often results in dendritic elongation (Pyapali and Turner, 1996). Such elongation results in a straightening of dendritic paths with regrowth (Fig. 6).

Functional implications

Although neurons are routinely studied physiologically, there remain many uncertainties in the relation between cellular function and structure. These include at the most basic level the passive electrotonic structure of the cell, which is determined by its geometric structure and specific membrane properties (Carnevale et al., 1997; Mainen et al., 1996; Major et al., 1994; Spruston et al., 1994; Turner, 1984a). Our present data confirm that there are large differences in dendritic electrotonic attenuation, considered both as signals propagating from the soma to the terminals and from terminals to the soma. The significant asymmetry of the signal transfer in the two directions points to the cellular processing and integration of synaptic and threshold electrical events, which differ considerably between the hippocampal cell classes. The most common physiologic signal for propagation into dendritic branches from the soma is an action potential, the presence or absence of which may critically influence dendritic synaptic function due to the enhanced depolarization (Yuste and Tank, 1996). However, the poor propagation of synaptic dendritic signals to the soma in pyramidal neurons suggests that dendritic integration is biased away from single synapses but instead requires the convergence of multiple synapses for threshold-level depolarization to occur (Turner, 1984b). However, other features of dendritic signal processing, particularly the presence of spines and voltage-gated channels, which are beyond the scope of the present study, must be included to understand better the interplay of geometry and membrane properties.

LITERATURE CITED

Alcantara S, Ruiz M, Darcangelo G, Ezan F, Delecea L, Curran T, Sotelo C, Soriano E. 1998. Regional and cellular patterns of reelin mRNA expression in the forebrain of the developing and adult mouse. J Neurosci 18:7779–7799.

Bower JM, Beeman D. 1994. The Book of Genesis; exploring realistic neural models with the general neural simulation system. Los Angeles: Teleos Publishing.

Cannon RC, Turner DA, Pyapali GK, Wheal HV. 1998. On-line archive of reconstructed hippocampal neurons. J Neurosci Methods 84:49–54.

Carnevale NT, Tsai KY, Claiborne BJ, Brown TH. 1997. Comparative electrotonic analysis of three classes of rat hippocampal neurons. J Neurophysiol 78:703–720.

Carriquiry AL, Ireland WO, Kleimann W, Uemura E. 1991. Statistical evaluation of dendritic growth models. Bull Math Biol 53:579–590.

Caserta F, Eldred WD, Fernandez E, Hausman RE, Stanford LR, Bulderev SV, Schwarzer S, Stanley HE. 1995. Determination of fractal dimension of physiologically characterized neurons in two and three dimensions. J Neurosci Methods 56:133–144.

Henze DA, Cameron WE, Barrionuevo G. 1996. Dendritic morphology and its effects on the amplitude and rise-time of synaptic signals in hippocampal CA3 pyramidal cells. J Comp Neurol 369:331–344.

Ireland W, Heidel J, Uemura E. 1985. A mathematical model for the growth of dendritic trees. Neurosci Lett 54:243–249.

Ishizuka N, Cowan WM, Amaral DG. 1995. A quantitative analysis of the dendritic organization of the pyramidal cells in the rat hippocampus. J Comp Neurol 362:17–45.

Jelinek HF, Fernandez E. 1998. Neurons and fractals: how reliable and useful are calculations of fractal dimensions? J Neurosci Methods 81:9–18.

Kliemann WA. 1987. Stochastic dynamic model for the characterization of the geometrical structure of dendritic processes. Bull Math Biol 49:135–152.

Li XG, Somogyi P, Ylinen A, Buzsaki G. 1994. The hippocampal CA3 network: an in vivo intracellular labeling study. J Comp Neurol 339:181–208.

Major G, Larkman AU, Jonas P, Sakmann B, Jack JJB. 1994. Detailed passive cable models of whole-cell recorded CA3 pyramidal neurons in rat hippocampal slices. J Neurosci 14:4613–4638.

Mainen ZF, Carnevale NT, Zador AM, Claiborne BJ, Brown TH. 1996. Electronic architecture of hippocampal CA1 pyramidal neurons based on three-dimensional reconstructions. J Neurophysiol 76:1904–1923.

Migliore M, Cook EP, Jaffe DB, Turner DA, Johnston D. 1995. Computer simulations of morphologically reconstructed CA3 hippocampal neurons. J Neurophysiol 73:1157–1168.

Mott D, Turner DA, Okazaki M, Lewis DV. 1997. Interneurons of the dentate-hilus border of the rat dentate gyrus: morphological and electrophysiological heterogeneity. J Neurosci 17:3990–4005.

Nedivi E, Wu G-Y, Cline HT. 1998. Promotion of dendritic growth by CPG15, an activity-induced signaling molecule. Science 281:1863–1866.

Pyapali GK, Turner DA. 1994. Denervation-induced alterations in CA1 pyramidal neurons following kainic acid lesions in rats. Brain Res 652:279–290.

Pyapali GK, Turner DA. 1996. Increased dendritic extent in CA1 hippocampal pyramidal cells from aged F344 rats. Neurobiol Aging 17:601–611.

Pyapali GK, Turner DA, Madison RD. 1994. Fetal transplants in rat hippocampus following kainic acid lesions: influence of post-lesion delay on graft survival and integration. Restor Neurol Neurosci 6:113–126.

Pyapali GK, Laslo A, Buzsaki G, Turner DA. 1998a. Dendritic properties of rat hippocampal dentate granule cells intracellularly labeled with biocytin in vivo. Soc Neurosci Abstr 24:60.

Pyapali GK, Penttonen M, Sik A, Buzsaki G, Turner DA. 1998b. Dendritic properties of intracellularly-stained rat hippocampal CA1 pyramidal neurons recorded in vivo and in vitro. J Comp Neurol 391:335–352.

Shetty AK, Madison RD, Bradley J, Turner DA. 1994. 5′Bromodeoxyuridine labeling of fetal hippocampal cell transplants: labeling efficacy and survival of suspension grafts in normal hippocampus. Exp Neurol 126:205–224.

Shetty AK, Turner DA. 1998. In vitro survival and differentiation of neurons derived from epidermal growth factor-responsive postnatal hippocampal stem cells: inducing effects of brain derived neurotrophic factor. J Neurobiol 35:395–425.

Sholl DA. 1953. Dendritic organization in the neurons of the visual and motor cortices of the cat. J Anat 87:387–406.

Smith TG Jr, Lange GD, Marks WB. 1996. Fractal methods and results in cellular morphology—dimensions, lacunarity and multifractals. J Neurosci Methods 69:123–136.

Spruston N, Jaffe DB, Johnston D. 1994. Dendritic attenuation of synaptic potentials and currents: the role of passive membrane properties. TINS 17:161–166.

Spruston N, Jaffe DB, Williams SH, Johnston D. 1993. Voltage and space-clamp errors associated with the measurement of electrotonically remote synaptic events. J Neurophysiol 70:781–802.

Stanfield BB, Cowan WM. 1979. The morphology of the hippocampus and dentate gyrus in normal and reeler mice. J Comp Neurol 185:393–422.

Tamori Y. 1993. Theory of dendritic morphology. Phys Rev E 148:3124–3129.

Turner DA. 1984a. Segmental cable evaluation of somatic transients in guinea-pig hippocampal neurons (CA1, CA3 and dentate). Biophys J 46:73–84.

Turner DA. 1984b. Conductance transients onto dendritic spines in a segmental cable model of CA1 and dentate hippocampal neurons. Biophys J 46:85–96.

Turner DA, Wheal HV, Cole H, Stockley EW. 1991. Three-dimensional reconstructions and analysis of the cable properties of neurones. In: Chad J, Wheal HV, editors. Cellular neurobiology. Oxford: Oxford University Press p 225–246.

Turner DA, Li X-G, Pyapali GK, Ylinen L, Buzsaki G. 1995. Morphometric and electrical properties of reconstructed CA3 hippocampal neurons recorded in vivo. J Comp Neurol 356:580–594.

Turner DA, Buhl EH, Halier NP, Nitsch R. 1998. Morphological features of the entorhinal hippocampal connection. Prog Neurobiol 55:537–562.

Uemura E, Carriquiry A, Kliemann W, Goodwin J. 1995. Mathematical modeling of dendritic growth in vitro. Brain Res 671:187–194.

Uylings HBM, Ruiz-Marcos A, Pelt JV. 1986. The metric analysis of three-dimensional dendritic tree patterns: a methodological review. J Neurosci Methods 18:127–151.

Van Ooyen A, Van Pelt J, Corner MA. 1983. Implications of activity dependent neurite outgrowth for neuronal morphology and network development. J Theor Biol 172:63–82.

Van Pelt J. 1997. Effect of pruning on dendritic tree topology. J Theor Biol 186:17–32.

Van Pelt J, Verwer RWH. 1985. Growth models (including terminal and segmental branching) for topological binary trees. Bull Math Biol 47:323–336.

Van Pelt J, Dityatev AE, Uylings HBM. 1997. Natural variability in the number of dendritic segments: model-based inferences about branching during neurite outgrowth. J Comp Neurol 387:325–340.

Woldenberg MJ, O'Neill MP, Quackenbush LJ, Pentney RJ. 1993. Models for growth, decline and regrowth of the dendrites of rat Purkinje cells induced from magnitude and link-length analysis. J Theor Biol 182:403–429.

Yuste R, Tank DW. 1996. Dendritic integration in mammalian neurons, a century after Cajal. Neuron 16:701–16.

Zador AM, Agmon-Snir H, Segev I. 1995. The morphoelectrotonic transform: a graphical approach to dendritic function. J Neurosci 15:1669–1682.

Zafirov S, Heimrich B, Frotscher M. 1994. Dendritic development of dentate granule cells in the absence of their specific extrinsic afferents. J Comp Neurol 345:472–480.